Research paper

Assessing the origin and velocity of Ca^{2+} waves in three-dimensional tissue: Insights from a mathematical model and confocal imaging in mouse pancreas tissue slices

Marko Šterk [a,b], Jurij Dolenšek [a,b,c], Lidija Križančić Bombek [a,b,c], Rene Markovič [b,d], Darko Zakelšek [b], Matjaž Perc [b,e,f], Viljem Pohorec [a,b], Andraž Stožer [a,c,*], Marko Gosak [a,b,*]

[a] Institute of Physiology, Faculty of Medicine, University of Maribor, Taborska 8, SI-2000 Maribor, Slovenia
[b] Faculty of Natural Sciences and Mathematics, University of Maribor, Koroška cesta 160, SI-2000 Maribor, Slovenia
[c] Faculty of Arts, University of Maribor, Koroška cesta 160, SI-2000 Maribor, Slovenia
[d] Faculty of Electrical Engineering and Computer Science, Institute for Mathematics and Physics, University of Maribor, Koroška cesta 46, SI-2000 Maribor, Slovenia
[e] Department of Medical Research, China Medical University Hospital, China Medical University, Taichung, Taiwan
[f] Complexity Science Hub Vienna, 1080 Vienna, Austria

ARTICLE INFO

ABSTRACT

Many tissues are gap-junction-coupled syncytia that support cell-to-cell communication via propagating calcium waves. This also holds true for pancreatic islets of Langerhans, where several thousand beta cells work in synchrony to ensure proper insulin secretion. Two emerging functional parameters of islet function are the location of wave initiator regions and the velocity of spreading calcium waves. High-frequency confocal laser-scanning imaging in tissue slices is one of the best available methods to determine these markers, but it is limited to two-dimensional cross-sections of an otherwise three-dimensional islet. Here we show how mathematical modeling can significantly improve this limitation. Firstly, we analytically determine the shape of velocity profiles of spherical excitation waves in the focal plane of a homogeneous three-dimensional space. Secondly, we introduce a mathematical model consisting of coupled excitable cells that considers cellular heterogeneities to approach more realistic conditions by means of numerical simulations. We demonstrate the effectiveness of our approach on experimentally recorded waves from an islet that was stimulated with 9 mM glucose. Furthermore, we show that calcium waves were primarily triggered by a specific region located 30 μm bellow the focal plane at the periphery of the islet. Additionally, we show that the velocity of the calcium wave was around 80 μm/s. We discuss the importance of our approach for the correct determination of the origin and velocity of calcium waves from experimental data, as well as the pitfalls that are due to improper procedural simplifications.

© 2020 Elsevier B.V. All rights reserved.

---

* Corresponding authors at: Faculty of Medicine, University of Maribor, Taborska 8, SI-2000 Maribor, Slovenia.
E-mail addresses: andraz.stozer@um.si (A. Stožer), marko.gosak@um.si (M. Gosak).

1. Introduction

Already in 1883, Ca^{2+} ions were identified as an essential and ubiquitous intracellular messenger [1]. More than a century later, the search for molecular and cellular mechanism of Ca^{2+} signaling are still ongoing. A major breakthrough in the quest was the development of Ca^{2+}-sensitive dyes and imaging techniques that helped to elucidate the role of Ca^{2+} ions as a most versatile secondary messenger regulating processes as diverse and universal as fertilization, cell cleavage, development, contraction, secretion, and cell death [2–5]. Since Ca^{2+} is a simple ion with binding sites on a plethora of target molecules, it cannot serve as a signal merely by its presence or specific binding. Instead, the information it carries is encoded in spatial and temporal patterns, which take the form of intracellular oscillations and waves [6,7]. Intercellular Ca^{2+} waves of different shapes, directions and frequencies, that are mediated by different mechanisms are crucial for the coordinated function of coupled cells in a number of different tissues [7–9].

In the strict sense, the term intercellular Ca^{2+} waves is reserved for non-excitable cells where the waves occur on a temporal scale of several seconds, and spread between a few, tens, or hundreds of cells with a velocity of around 10-30 μm/s, consistent with the diffusion of messengers [10]. In the broader sense, a number of electrically excitable cells are coupled via gap junctions and depolarization waves spreading between cells are often followed by Ca^{2+} increases in these cells, giving the appearance of Ca^{2+} waves. Typically, these waves occur on a temporal scale of 1 second or less, encompass up to thousands of cells and are typically faster (> 30 μm/s), do not show delays, and rely mechanistically on depolarizing electrical currents [6,7,9].

Nevertheless, irrespective of the cell type intercellular waves have the same crucial task, i.e., to help cells overcome differences in their sensitivity and produce a synchronized response [7]. One of the most fascinating aspects of intercellular Ca^{2+} dynamics is that local activity in a population of heterogeneous cells embedded in a changing and noisy environment can be organized into complex and rather regular spatiotemporal patterns, which facilitate the transfer of information. Not only are these structures physiologically important, they are also theoretically appealing and challenging to understand. As a result, numerus computational models have been developed to support experimental endeavors and to elucidate the underlying mechanisms. For instance, previous studies have utilized models and simulations to identify the key intercellular messengers [11], to investigate the role of intercellular topology [12,13], to explore dynamical transitions and synchronization behavior [14,15], assess the velocity of signal propagation [16], to evaluate the effect of noise and cellular heterogeneity [17–19], and, of course, to investigate how they are regulated by mechanical and biochemical factors to maintain essential physiological functions [20]. Models have been developed for networks of non-excitable cells, such as endothelial [12] and epithelial [11] cells, keratinocytes [21], acinar cells [22], hepatocytes [23], and astrocytes [24], to name only a few examples. From the perspective of complexity, numerical simulations of coupled excitable cells are an even more challenging task. Computational studies of Ca^{2+} waves have plenty in common with the study of wave propagation in other excitable models, such as the Hodgkin-Huxley or FitzHugh-Nagumo models, and can predict very complex spatiotemporal patterns [25–27]. Until today, cell-specific models to study the collective Ca^{2+} activity have been mostly designed for various types of smooth muscle cells [28–32] and insulin-secreting beta cells from pancreatic islets of Langerhans [33–38].

The latter is a particularly interesting system to study intra- and intercellular Ca^{2+} signaling. A typical mouse islet is around 100 μm in diameter and consists of around 1000 cells of at least five different types, with the insulin secreting beta cells being the most prevailing in the islet core and representing around 60-80 % of all cells. In terms of composition and size, islets are highly heterogeneous, with some comprising only a few cells and some having diameters well above 500 μm [39]. Cells communicate with each other through different mechanisms; with gap-junctional coupling probably being the main synchronizing mechanism for depolarization and Ca^{2+} waves [40,41]. These microorgans are biologically highly complex [42,43], accessible to advanced modelling, experimental, and analytical approaches [44–46], and their disruption leads to type 2 diabetes mellitus, which is increasingly becoming an important public health problem [47,48]. When exposed to stimulatory glucose concentrations, mouse beta cells in isolated islets and pancreatic tissue slices exhibit a multimodal oscillatory pattern. The slow oscillatory component with a period of several minutes is believed to reflect glycolytic oscillations, whereas the superimposed fast component resembles a glucose-dependent electrical activity with a frequency of several oscillations per minute [49]. Both slow and fast oscillations are well synchronized between different beta cells of the same islet, predominantly by gap-junctional coupling through Connexin36, even though other means of intercellular communication probably contribute to intercellular Ca^{2+} wave generation as well [38,42,43,45,50–52]. The collective activity of slow oscillations has not yet been resolved conclusively and is probably driven by diffusion of the metabolic intermediate glucose-6-phosphate [53,54]. Synchronous behavior of fast oscillations is receiving much more attention from the scientific community and is governed by electrical depolarization, resulting in the appearance of Ca^{2+} waves that propagate across the islets [55–59].

Motivated by the fact that well-organized collective activity is a prerequisite for proper hormone secretion, *in silico* approaches are increasingly becoming an integral part in islet research [60–62]. Multicellular models incorporating either single cellular type (beta cells) or three cellular types (alpha, beta, and delta cells) are of paramount importance for exploring their synchronous behavior, Ca^{2+} wave propagation, and heterologous cell communication within the islet tissue [34,63–68]. In recent years, particular emphasis has been given to the incorporation of the well-known beta cell heterogeneity into beta cell models, as it has been shown to profoundly affect dynamical transitions and intercellular activity [14,69,70]. Studies utilizing a combination of experimental findings, advanced analyses, and computational models have revealed that Ca^{2+} waves originate from specific and rather randomly distributed subregions with elevated excitability [36,65,71]. Moreover,

recent research suggests that the multifaceted heterogeneity also includes cell-to-cell variability and a heterogeneous nature of intercellular interactions. Both must be included in computational models, in order to firmly reproduce experimentally observed collective beta cell behavior [36,37,72].

Several experimental studies have investigated the extent and mechanism of synchronicity between fast Ca^{2+} oscillations in beta cells. In isolated islets, the oscillations from different parts of the islets were found to be phase-shifted for up to 2 seconds [73]. Considering the characteristic size of the islets (100 μm), it could thus be estimated that the velocity of signal transmission was around 50-100 μm/s. Additionally, it was reported that the direction of the waves might change from one oscillation to another [73]. Moreover, similar results were obtained in clusters of beta cells [74], isolated mouse [75] and human [76] islets and in islets *in vivo* [77–79], but, remarkably, neither of the studies explicitly mentioned intercellular Ca^{2+} waves. Similar values were also obtained with electrophysiological experiments [80]. A more explicit Ca^{2+} imaging and simulation study by Aslanidi et al. [33] provided first convincing evidence for depolarization front-dependent Ca^{2+} waves, quantified the relationship between gap junctional coupling, membrane conductance, and wave velocity, and concluded that the predicted wave velocities are typically between 30 and 100 μm/s in glucose-stimulated islets. Later, Benninger et al. [34] provided a decisive piece of evidence for the dependence of Ca^{2+} waves on gap junctions and depolarization in isolated islets and that a genetic disruption of connexin 36 slows and disrupts Ca^{2+} waves. The estimated wave velocities were between 20 and 200 μm/s and the observed directions of spreading were not always the same. Interestingly, Cappon and Pedersen [69] also demonstrated numerically that the wave velocity is a function of the average gap junctional conductance, which holds true also in ensembles of heterogeneous networks of beta cells.

We would like to conclude this brief review of previous findings by pointing out some promising recent studies that assessed the velocity of Ca^{2+} waves *in vivo* in zebrafish islets, islets transplanted into the anterior chamber of the eye, and in exteriorized pancreata, some even in all three dimensions (3D) [79,81–83]. However, according to the available information, none of the studies so far primarily addressed the problem of true wave origin and velocity in 3D tissue and the abovementioned studies were limited by rather low temporal resolutions. More precisely, both tissue slices and islets are 3D. Imaging methods to detect Ca^{2+} waves enable one to detect Ca^{2+} changes predominantly in the stronger stained periphery of isolated islets and in the part of the islet closer to the objective in the case of a camera-based system, or in an approximately 5 μm thick focal plane in case of confocal microscopy. Thus, velocities calculated by simply dividing the distances between wave origins and ends by phase lags are probably imprecise estimates. Moreover, true origins and ends of waves could lie outside the recorded area. Finding true wave-initiating regions is especially important in the light of recent findings that pacemakers might exhibit metabolic features different from follower cells and other specialized cells [41,43,82,84]. Typically, pacemakers are found at the periphery of islets, which may be the result of peripheral cells being exposed to glucose sooner than other cells in some experimental settings, a true biological heterogeneity in some metabolic parameters, being coupled to fewer neighboring cells, or due to a combination of these factors [33–36,72]. However, sometimes they appear to be located more centrally, but this could also be an experimental artefact. Finally, understanding the spreading of waves in 3D could also help us resolve some previous findings of complete synchronicity between cells as well as the findings that some cells, called hub cells, are strongly synchronized with many other cells [85].

The main goal of this study was therefore to investigate how the Ca^{2+} wave velocity can be computed based on multicellular Ca^{2+} imaging and to determine the distribution of wave origins in 3D space. To this end, we combined theoretical models and simulations with experimental observations. With respect to the latter, we limit ourselves to tissue slices and confocal microscopy, but one shall easily extrapolate our findings to other models and modes of recording. We resorted to theoretical models to gain quantitative insight as our and other experimental setups do not yet make the observation of intracellular Ca^{2+} changes possible in 3D. In particular, we first considered the spread of spherical excitation waves in homogeneous 3D space to determine analytically the shapes of velocity profiles in the focal plane. Then, we built multicellular models of coupled excitable cells to examine this issue by means of numerical simulations, also in the scenario which included realistic physiological determinants, such as cellular heterogeneity. Finally, we used the acquired insights from theoretical and numerical models to analyze experimental data and to determine the Ca^{2+} wave velocity and the spatial distribution of wave initiators within the islet.

2. Materials and methods

2.1. Numerical model of wave propagation in a homogeneous excitable lattice

For numerical simulations of excitation wave propagation in a homogeneous lattice of coupled cells, we utilized the two-dimensional Rulkov iterative map, a phenomenological model of excitable cellular oscillators. It was first proposed by Rulkov [86] for modelling of spiking-bursting neural behavior but it lends itself well for modeling of other types of excitable cells, including beta cells [72]. It consists of two iterative equations:

$$u_{i,j,k}(n+1) = \frac{\alpha_{i,j,k}}{1 + u_{i,j,k}(n)^2} + v_{i,j,k}(n) + gK_{i,j,k}, \tag{1}$$

$$v_{i,j,k}(n+1) = v_{i,j,k}(n) - \sigma u_{i,j,k}(n) - \chi, \tag{2}$$

where $u_{i,j,k}(n)$ and $v_{i,j,k}(n)$ are, respectively, the slow and the fast dynamical variable at iteration step n for the cell at the given grid location $i,j,k=1,....,17$. The (x,y,z) coordinates for each cell were then determined by mapping the (i,j,k) grid system to the unit cube with equidistant grid spacing 1/17. In a biological sense, the variable $u_{i,j,k}(n)$ mimics the membrane potential and the variable $v_{i,j,k}(n)$ emulates the dynamics of gating variables. Both are considered as dimensionless quantities. Of special importance are the parameter $\alpha_{i,j,k}$ which defines the dynamical regime [72,86], and the last term of Eq. (1) which represents the diffusive intercellular coupling between neighboring cells ($K_{i,j,k}$). The latter is realized by a finite difference scheme using a 19-point stencil:

$$K_{i,j,k} = \frac{1}{8}\Big[u_{i+1,j,k+1} + u_{i-1,j,k+1} + u_{i+1,j,k-1} + u_{i-1,j,k-1} + u_{i+1,j+1,k} + u_{i-1,j+1,k} + u_{i+1,j-1,k}$$
$$+ u_{i-1,j-1,k} + u_{i,j+1,k+1} + u_{i,j-1,k+1} + u_{i,j+1,k-1} + u_{i,j-1,k-1} + 4\big(u_{i+1,j,k} + u_{i-1,j,k} + u_{i,j+1,k}$$
$$+ u_{i,j-1,k} + u_{i,j,k+1} + u_{i,j,k-1}\big) - 36u_{i,j,k}\Big]. \tag{3}$$

It should be noted that by applying this finite difference approximation, we formally treat the lattice as a discretization of continuous excitable media. No-flux boundary conditions were applied at the edges. With 17 cells along each axis we used 4913 cells. It should be noted that both the model and the experimentally used islet are larger than average islets, but in good agreement with each other. This size was chosen for easier visualization and better quantification of phase lags and velocity profiles. The value of parameter $\alpha_{i,j,k}$ was the same for all cells ($\alpha_{i,j,k} = 1.98$), putting them into an excitable regime, except for cells which were chosen as so-called pacemakers. These chosen cells were placed at the bottom of the system at the middle of the xy plane as specified by indices ($8 \le i, j \le 10$) and ($0 < k \le 3$) with $\alpha_{i,j,k} = 2.1$, thereby exhibiting oscillatory dynamics leading to initiation of propagating waves. Other system parameters were $\chi = \sigma = 0.001$ and $g = 0.007$.

2.2. Numerical model of wave propagation in a heterogeneous network of cells

To build a biologically more relevant tissue architecture, we constructed the network by assigning each cell a random set of coordinates in a unit cube while considering the restraint that two cells cannot be closer to each other than a predefined threshold distance ($d_{th} = 0.05$). The number of cells was the same as in the lattice network (N=4913). Once all cells were placed in the network connections between cells were established. If the coordinates of a pair of cells were within a predefined radius r, there were considered connected. This radius was determined iteratively to ensure that the average number of connections in the system is biologically relevant, i.e. around 8 [38,69,87–89]. To simulate the dynamics of each node we utilized again the Rulkov oscillator model [86], similarly as described above:

$$u_i(n+1) = \frac{\alpha_i}{1 + u_i(n)^2} + v_i(n) + g \sum_j C_{i,j}\big[u_j(n) - u_i(n)\big], \tag{4}$$

$$v_i(n+1) = v_i(n) - \sigma u_i(n) - \chi. \tag{5}$$

The last term in Eq. (4) represents the coupling between the i-th cell to all its neighbors and the parameter $C_{i,j}$ describes the coupling strength between the i-th and j-th cell. Pancreatic beta cells exhibit different facets of heterogeneity [60]. We incorporated this important aspect into our model by randomly distributing $C_{i,j}$ between 0.8 and 1.2 in order to simulate heterogeneity of intercellular coupling while the coupling parameter was set to g=0.02. Moreover, to account for cell-to-cell variability of electrical excitability, the values α_i were randomly assigned from the interval between 1.98 and 1.99, except for the pacemaker cells, where we set $\alpha_i = 2.1$. The pacemakers were again set approximately at the middle of the xy plane at the bottom of the system in the region ($0.47 \le x, y \le 0.53$) and ($0 \le z \le 0.1$).

2.3. Experimental methods

Acute 140 μm thick pancreatic tissue slices sized 1-3 mm^2 were prepared from a 13 week old male NMRI mouse employing the same tissue extraction and preparation steps as well as solutions as published previously [90,91]. All experiments were conducted in strict accordance with the national and European recommendations concerning experimental animals. For confocal functional multicellular Ca^{2+} imaging (fMCI), slices were transferred into a bath chamber at 37°C continuously perfused with carbogen-bubbled (5% CO$_2$, 95% O$_2$) extracellular solution (ECS) mounted on Leica TCS SP5 AOBS Tandem II upright confocal microscope system using a Leica HCX APO L water immersion objective (20 x, NA=1.0). Fluorophore Oregon green BAPTA-1 (OGB-1) was excited with 488 nm argon laser and the fluorescence detected with Leica HyD hybrid detector in the range of 500–700 nm (all from Leica Microsystems GmbH, Wetzlar, Germany). Images were acquired from a 5 μm thick optical layer approximately 20 μm below the cut surface to avoid imaging from the most damaged layer [91]. The resolution was set to 8-bit 256 × 256 pixels @ 10 Hz allowing discrimination of individual Ca^{2+} oscillation at single cell resolution. Prior to and following time series acquisition, a reference high-resolution image (1024 × 1024 pixels) was taken to account for potential motion artefacts during off-line analysis. The stimulation protocol consisted of non-stimulatory 6 mM glucose in ECS for the first 2 minutes, followed by 9 mM glucose in ECS persisting for 40 minutes. A representative slice with 207 beta cells was selected for further analyses; 22 cells were excluded from further analysis due to not-sufficient signal-to-noise ratio.

2.4. Data processing

All recorded time series were first band-pass filtered to remove noise, baseline drift and to extract the fast component of Ca^{2+} oscillations. The frequency band of interest was chosen by visual assessment between 0.06 Hz and 1.0 Hz. After filtration the time series were smoothed by a standard sliding-window algorithm and binarized cellular activity was extracted for each cell. The extracted binarized cellular signals were the foundation for further analysis. Numerical simulations yielded binarized signals by simply thresholding the amplitude of the fast component variable. If the amplitude of the fast component exceeded a predetermined value of ($u_i(n) = -0.4$) the cell was deemed active. No additional pre-processing steps were required for data obtained from numerical simulations.

Individual Ca^{2+} waves were detected by analyzing the binarized signals of all cells. Cells i and j were deemed to be part of the same event if the following criteria were met:

$$\left| T_i - T_j \right| < T_{th},$$

$$d_{i,j} < R_{th}^{wave},$$

where T_i and T_j are the activation times of the i-th and j-th cell, T_{th} is a pre-set threshold time, $d_{i,j}$ is the Euclidian distance between the i-th and j-th cell and R_{th}^{wave} is a pre-set threshold distance between cells, similarly as described previously [36]. The threshold time was set to $T_{th} = 0.5\ s$ for experimental data and $T_{th} = 200$ (a.u.) for numerical simulation data, and the threshold distance was set to $R_{th}^{wave} = 40\ \mu m$ for experimental data and $R_{th}^{wave} = 0.06$ (a.u.) for numerical simulation data. If, for example, cells i and j were close enough together (condition ii) and cell i activated just slightly before cell j (condition i), it was deemed that the signal travelled from cell i to cell j and the two cells were thus considered to be part of the same event. With this algorithm we detected the activation sequences of all cells in the islet (experimental data) and all cells in a chosen slice of the numerical model (at a chosen z coordinate).

3. Results

3.1. Theoretical considerations

3D excitation waves in pancreatic islets can be experimentally assessed only in 2D cross-sections, but they can be triggered anywhere outside this focal plane. Here we examined the shape of wave velocity profiles in one plane as a function of the wave origin location. We derived a simple theoretical model of 3D wave propagation using the following assumptions:

 i) The origin of the wave is directly beneath the first detected activity in the observed (focal) plane. With this we assume that the tissue is homogeneous and isotropic, thereby leading to ideal spherical geometry of the excitation wavefront, which hits the focal plane first directly above the initiating region.
 ii) Wave front propagation velocity is uniform and constant. This reflects the scenario of cells being packed tightly together forming a perfect regular lattice, with each of them having the same coupling strength.
iii) Waves propagate outwards from the point of origin in the form of concentric spheres and do not produce reflections when they hit the edge of the system. This reflects authentic behavior in excitable tissue, as the excitation waves diminish once they arrive at the boundaries.

It should be noted that assumptions i) and ii) symbolize a very simplified description of the real tissue, but are nonetheless at this stage required for the theoretical formulation. In continuation, we will therefore address the more realistic scenario with numerical simulations.

Once the wave front, which originates from (x_{or}, y_{or}, z_{or}), hits the observed (focal) plane it propagates outwards from the point of impact (x_{or}, y_{or}, z') in the form of concentric circles, as presented in Fig. 1A and Supplementary video 1. The wave front hits point (x', y', z') in the observed plane once the wave front has travelled the distance L. Considering assumptions i) and ii), we can express the travelled distance (L) of the wave front as:

$$L = ct, \tag{6}$$

where c is the constant wave front velocity and t is time. Furthermore, we can express the travelled distance in terms of the coordinates of the projected wave front onto the observed (focal) plane as:

$$L = \sqrt{r'^2 + z'^2}, \tag{7}$$

where r' is the radial distance from the point of impact on the observed plane Fig. 1A) and can be expressed as $r' = \sqrt{x'^2 + y'^2}$. By equaling Eqs. (6) and ((7), considering z' as a constant, and taking the time derivative, we derive:

$$v(r') = \frac{c}{r'}\sqrt{r'^2 + z'^2}, \tag{8}$$

where $v(r')$ is the wave front propagation velocity on the observed plane as a function of the radial distance from the point of impact. It can be noticed that if $r \to 0$ then $v \to \infty$ and if $r \to \infty$ then $v \to c$. Velocity profiles as a function of the radial distance from the impact point are presented in Fig. 1B and C, for different depths z'.
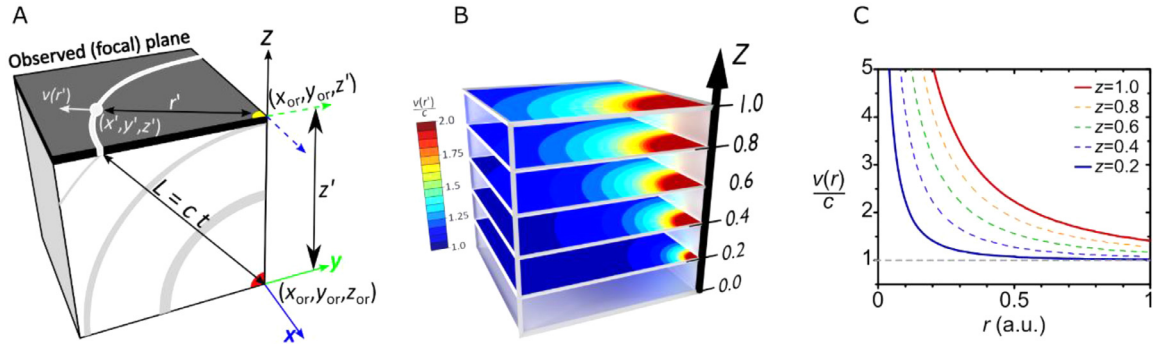
Fig. 1. A) A schematic representation of propagating concentric spherical waves emanating from the point of origin (red dot) at coordinates x_{or}, y_{or} and z_{or} with a wave-front velocity c. L is the travelled distance of the wave in time t. Observed (focal) plane at coordinate z' above the point of origin and starting point of the wave on this plane (yellow dot) with coordinates x_{or}, y_{or} and z'. Shown is the projection of the 3D wave front onto the 2D plane (circle – white) at a radius r' and projected wave velocity $v(r)$ at coordinates x', y' and z'. B) Surface plots showing the spatial profile of the normalized wave velocities ($v(r')/c$) on multiple observed (focal) planes. C) The circularly-averaged velocity profiles as a function of the radial distance (r') for observed (focal) planes at different z coordinates ($z=0.2$, $z=0.4$, $z=0.6$, $z=0.8$ and $z=1.0$).

Eq. (8) describes the wave propagation velocity in the observed plane as a function of the radial distance, however, if the values of the wave propagation velocity profile are known we can calculate the height of the observed plane above the point of origin. We can do this by rearranging Eq. (8) and expressing z' as:

$$z' = \frac{r'}{c}\sqrt{v(r)^2 - c^2}. \tag{9}$$

Using Eq. (9), our first assumption and the calculated velocity profiles along the observed plane, we can calculate the point of origin of each detected wave.

4. Numerical results

4.1. Excitation wave propagation in a 3D lattice of homogeneous excitable cells

Firstly, we simulated the excitation wave propagation in a 3D lattice of excitable cells to examine how the wave behavior matches theoretical considerations. The coordinates of the grid element (i,j,k) were uniformly placed within a unit cube, with the lattice distance 1/17. The arrangement is visualized in Fig. 2A. The dynamics of the (i,j,k) grid element was governed by the Rulkov map model, as described in the Methods section. Pacemaker cells were placed at the bottom of the system in the middle of the *xy (ij)* plane. The arrangement is visualized in Fig. 2A. Temporal traces from these two cells are shown in the upper panel of Fig. 2B, whereas the lower panel in Fig. 2B features the onsets of oscillations of all cells, color-coded in accordance with their relative activation time within the given wave (red cells activated first and blue cells activated last). The cells are indexed with respect to their distance from the center, i.e., first-responder. The monotonic inclination of points indicates that the excitation signal was a regular concentric wave traveling from the center to the boundary, as we describe in more detail bellow.

Propagation of an excitation wave in the chosen plane ($z \approx 0.82$, $k=14$) of the 3D lattice is visualized in Fig. 3 in the form of subsequent snapshots at equally spaced iteration steps ($n=0$, $n=6$, $n=12$ and $n=18$), whereby the grey dots reflect inactive cells, while red and orange cells reflect newly active and previously active cells, respectively. It can be inferred that the wave propagated faster in the initial moments after impact compared to later iteration steps, which corresponds well to theoretical predictions presented in section Theoretical considerations. This observation is further corroborated by the Supplementary Video S2.

To assess the differences between the velocity profiles in different planes of the 3D lattice, we analyzed cellular activity in different planes above the initiating region. The resulting activation profiles are shown in the upper panels of Fig. 4 for $z \approx 0.06$ ($k=2$), $z \approx 0.41$ ($k=7$), and $z \approx 0.82$ ($k=14$). Evidently, the wave front propagates much faster when the planes are further away from the origin of the wave, as predicted theoretically. The velocity profiles were calculated by dividing the planes into 6 (or 5) concentric circular sectors of width 0.12 (or 0.14) with the center in the middle where the first cells responded (black cross), as presented in the upper panels in Fig. 4. Each cell was assigned to a sector based on its radial distance from the starting point and the activation time for each sector was determined as an average of all cells within a given sector. Considering these average activation times and the distances between sectors, the velocity profile $v(r)$ was calculated (see Methods for details). As expected, the velocity profile in a given plane is a monotonically decreasing function of the radial distance converging to wave velocity c, which was measured to be $c=0.0024$ (a.u.) in the pacemaker plane. In particular, the actual wave front velocity was determined on the basis of the time required for the wave front to travel from the origin at the center to the edge in the second lowermost plane.
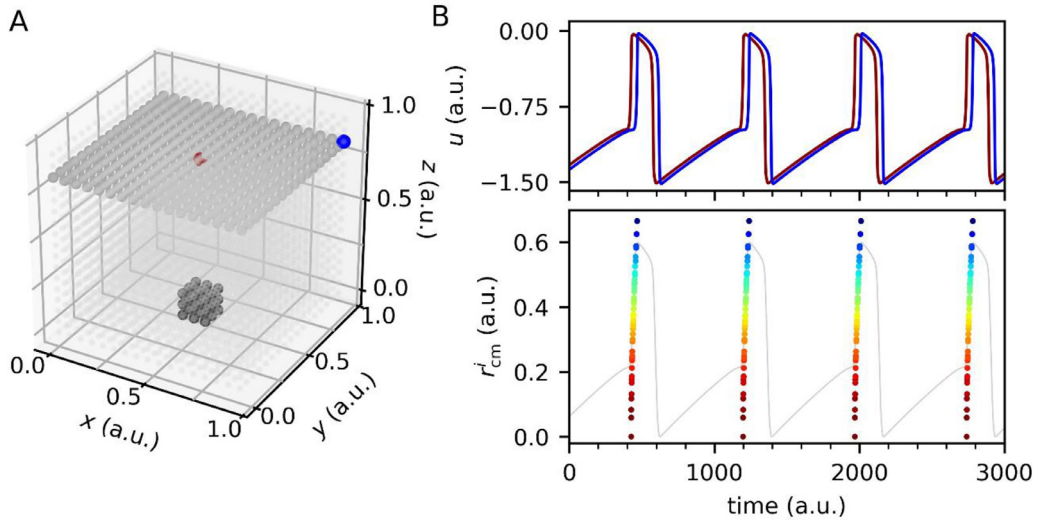
Fig. 2. A) The 3D lattice network of excitable cells. Pacemaker cells are shown at the bottom of the *xy (ij)* plane in black, cells in the chosen "focal" plane ($z\approx0.82$, $k=14$) are shown in grey, and all other cells are shown as light grey spheres. The first- and last-responding cells in the chosen plane are shown as red and blue spheres, respectively. There were $N=17$ cells placed within the unit interval along each axis. B) Time series of the first (red) and last (blue) responding cells in the observed plane, upper panel, and raster plot of the activation sequence of all cells in the chosen slice for all detected events sorted in accordance with the distance from first responder r_{cm}^i (red cells activated first and blue cells activated last). The light grey line in the lower panel shows the mean field signal of all cells in the chosen plane.
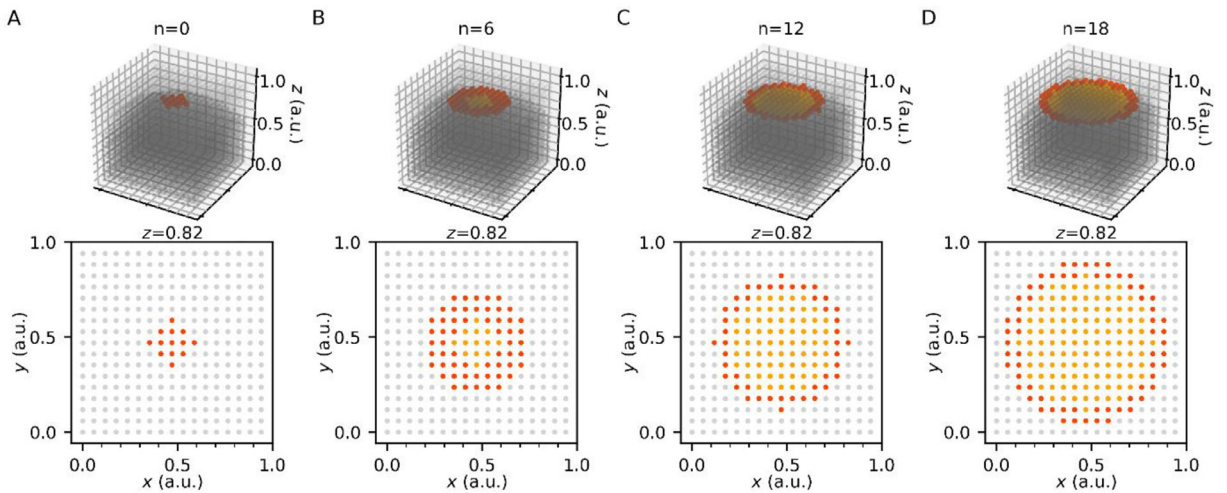
Fig. 3. Snapshots of excitation wave propagation in the 3D lattice (upper panels) and in the chosen plane at $z\approx0.82$ ($k=14$) (lower panels) for iteration steps $n=0$ (A), $n=6$ (B), $n=12$ (C), and $n=18$ (D) after the wave front hit the observed plane. Active cells in the 3D lattice are shown in black, inactive cells are shown in light grey, newly active cells in the chosen plane are shown in red and previously active cells are shown in orange.

4.2. Excitation wave propagation in a heterogeneous network of excitable cells

To simulate the cellular behavior in a biologically more relevant architecture of the beta cell network in pancreatic islets, we utilized a random geometric network to model intercellular interactions. Besides topological heterogeneity, we incorporated in our model cellular variability in terms of variable cell-to-cell coupling strengths and excitability levels, to account for the well-known beta cell heterogeneity (see Introduction and Materials and Methods). The spreading of the excitation wave initiated by the pacemaker region located at the bottom in the center of the *xy* plane is visualized in Fig. 5 as a series of equally spaced snapshots ($n=0$, $n=6$, $n=12$ and $n=18$). Similar as in the lattice model of coupled homogeneous cells, the wave propagated along the observed plane faster just after it hit the plane, but in this case, the wave front was rather distorted due to the abovementioned heterogeneities.

In Fig. 6 we present cellular activation profiles for three different slices located at $z=0.05$, $z=0.25$, and $z=0.5$, and the corresponding velocity profiles $v(r)$. Because of the integrated heterogeneities, the activation and velocity profiles were no
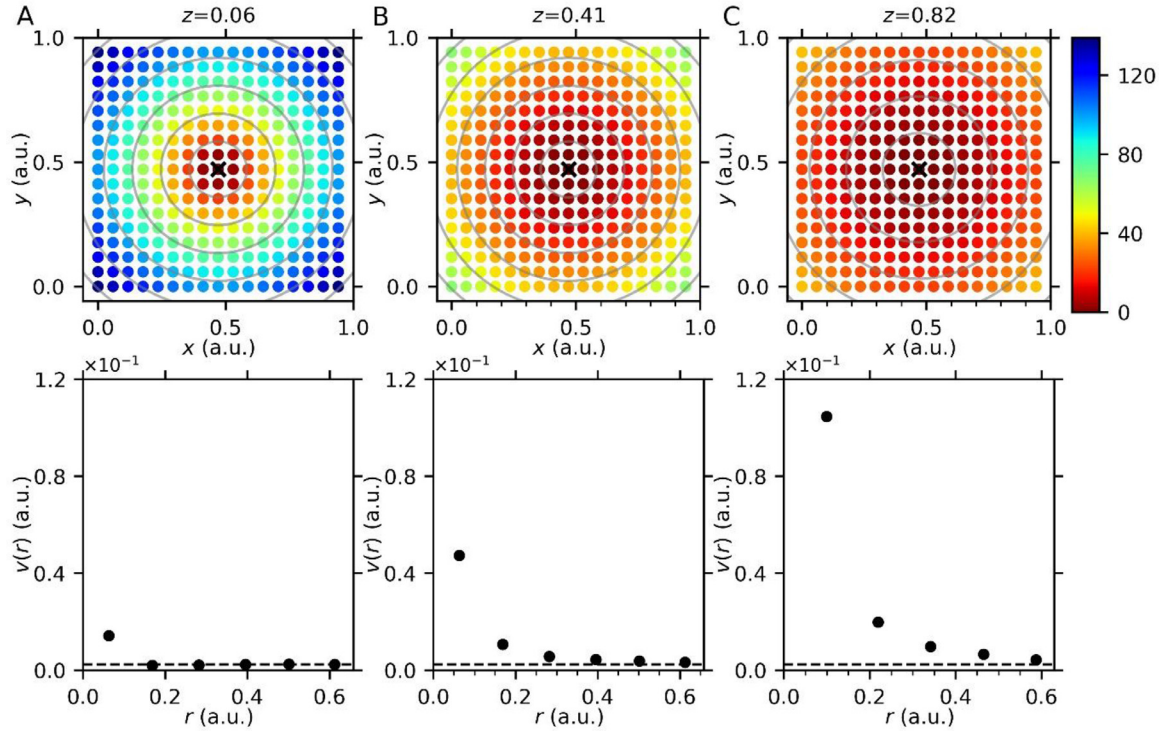
Fig. 4. Cellular activation profiles in different planes of the 3D lattice (upper panels) at $z \approx 0.06$ ($k=2$) (A), $z \approx 0.41$ ($k=7$) (B) and $z \approx 0.82$ ($k=14$) (C) with indicated wave starting locations (black crosses) and circular sectors (grey circles). Activation times of cells in each plane are color-coded, as indicated by the color bar. Lower panels feature their corresponding velocity profiles $v(r)$, i.e., velocities determined on the basis of average activation times in circular sectors and the distance from the origin. Dashed lines indicate the actual wave front propagation velocity (c), as determined in the pacemaker plane ($c = 0.0024$ a.u.).

longer as smooth as in the homogeneous lattice model, but the behavior was found to be qualitatively the same. The wave propagation was again found to be the fastest around the central area where the wave first hit the cross-section and this effect is more pronounced if the vertical distance from the wave origin is larger. Most importantly, towards the periphery of each plane, i.e., with increasing r, the wave propagation velocity in the slice invariably converged to the actual average velocity of the wave, which was determined in the pacemaker plane to be $c = 0.0029$ (a.u.). In particular, the actual wave front velocity was determined on the basis of the time required for the wave front to travel from the origin at the wave initiators located in the center to the edge in the slice located between $0.05 < z < 0.1$. The value was determined on the basis of the average of 5 different waves. A dynamic representation of the systems behavior is given in the Supplementary Video S3.

Next, we verified if the wave origin could be extracted in this model with incorporated heterogeneities. While in the 3D lattice of homogeneous cells the excitation waves were very regular and hence the pacemaker region could be determined very precisely, here, the waves are less coherent. To determine the origin of the wave we used the information about the average wave velocity c along with the x and y coordinate of the first responding cell(s) in the observed slice. The z coordinate was then determined by Eq. (9). In particular, to improve accuracy the vertical position of the initiator region was determined on the basis of the average over all 5 pairs of values of r' and $v(r')$. The results showing the inferred initiator regions for multiple waves are presented in Fig. 6D. Evidently, the extracted origins (green dots) are scattered around the actual initiator region (dark grey dots, i.e. pacemaker cells), but the origins could be determined quite precisely despite the erratic wave patterns caused by the heterogeneities. For the same reason, the extracted wave velocities are not always the same, as presented in Fig. 6E. The values are based on 50 different waves and are scattered around the mean value with a relative standard deviation of 16 %.

4.3. Analysis of experimental data

Fig. 7A shows a high-resolution image of the pancreatic tissue slice with the black line indicating the islet of Langerhans and cyan dots the positions of individual beta cells. We exported the Ca^{2+} time series of each cell and detected the onsets of individual oscillations. These data were further used to extract individual Ca^{2+} waves (see Materials and Methods). In the upper panel of Fig. 7B we show Ca^{2+} traces of the first- and last-responding cell in a detected Ca^{2+} wave and in the lower
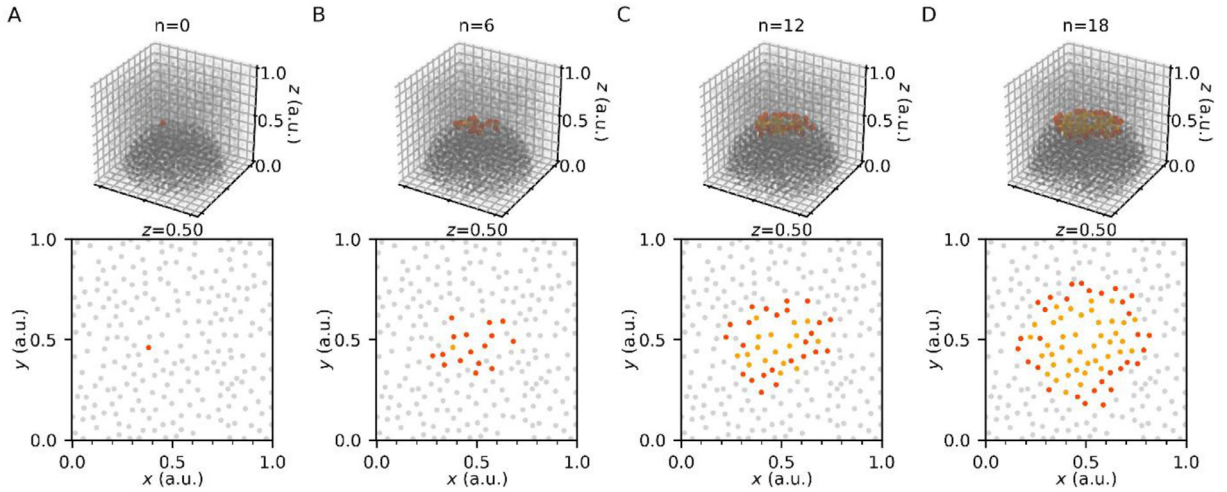
Fig. 5. Snapshots of excitation wave propagation in a heterogeneous network of coupled cells (upper panels) and in the *xy* projection of the chosen segment $0.48 \leq z \leq 0.52$ (lower panels) for iteration steps $n=0$ (A), $n=6$ (B), $n=12$ (C) and $n=18$ (D) after the wave front hit the observed slice. Active cells in the 3D network are shown in black, inactive cells are shown in light grey, newly active cells in the chosen slice are shown in red and previously active cells are shown in orange.

panel we present a raster plot of cellular activations for 4 subsequent Ca^{2+} waves. How the Ca^{2+} waves propagate across the islets is visualized in the Supplementary Video S4.

In the recording, 89 large scale waves were detected in which at least 45 % of all cells participated. For these events, we calculated the activation profiles and the corresponding average wave front propagation velocities as well as the origins of all waves. We used a similar approach as for the analysis of simulated data. For each wave, circular sectors were placed over the islet with the center at the first responding cell, as illustrated in Fig. 8A-C. The average activation time in an individual sector was then determined by all activation times in the given sector and of the neighboring sectors. This overlap was required to smooth the data, since due to a relatively small number of cells per sector and inherent noise the extracted profiles were quite erratic in some waves. Afterwards, profiles were visually inspected and those that were deemed unsuitable were discarded (15 wave profiles). In these waves, the velocity profiles were not decreasing functions of the distance from the impact point and contained multiple peaks. Most probably, distorted profiles are a consequence of multiple wave sources that triggered within a narrow time frame. As a result, we observe a superposition of multiple waves in the focal plane. We discuss this issue in more detail in the final section.

After selection, we used the remaining 74 wave profiles to calculate the wave velocity and the wave initiator regions. It should be noted that in some velocity profiles the values between sectors were rather similar, thereby indicating a constant velocity of wave propagation. Therefore, for waves in which the difference between the minimum and maximum values were less than 10 %, the origin was identified in the focal plane (6 waves). Activation profiles for 3 different waves from different depths are presented in Fig. 8 (upper panels), along with their velocity profiles, which specify the calculated velocity between two sectors in dependence on the distance from the wave impact point r (lower panels). The origin of the first wave (Fig. 8A) was in or slightly below the observed plane, because the velocity profile is nearly constant. For the second wave (Fig. 8B) the velocity profile is a moderately decreasing function of r, thereby indicating that the initiating region was further below the focal plane. In the case of the third wave (Fig. 8C) the detected velocity in the first sectors was significantly higher, thereby indicating that the wave originated from a deeper location within the islet. In Fig. 9A, the exact locations of these three waves are marked with colored stars.

In Fig. 9A the reconstructed positions of wave initiators are presented (green stars). The tissue slice is positioned at $z=0$ in the xy plane and beta cells are colored in accordance to their average activation time throughout all waves. The xy position of wave origin was determined based on the location, where the wave hit the focal plane. If multiple cells became activated simultaneously, the center of mass of all first responders was selected as the origin. The z position was obtained by Eq. (9), whereby the average wave velocity c was obtained as the average of the last two points in the velocity profiles (see dotted lines in Fig. 8), where we assume that the detected wave velocity roughly corresponds to the actual velocity. It turned out that a great proportion of waves originated from the same islet area located about 20 to 40 μm below the surface (Fig. 9B). Moreover, a large part of the waves was triggered from the periphery of the islet. To provide a rough quantification of this observation we calculated the locations of triggered waves as a function of the distance from the islet center in the slice (Fig. 9C). The latter was determined as the center of mass of all beta cell positions. In Fig. 9D the distribution of extracted velocities is shown for all 74 waves. The values are dispersed between 60 μm/s and 100 μm/s around the mean value of 82 μm/s. Noteworthy, 85 % of the values are between 70 μm/s and 90 μm/s. The dispersion is due to multiple factors, with wave front imperfections due to cellular heterogeneity and morphological distortions of islets being probably the most
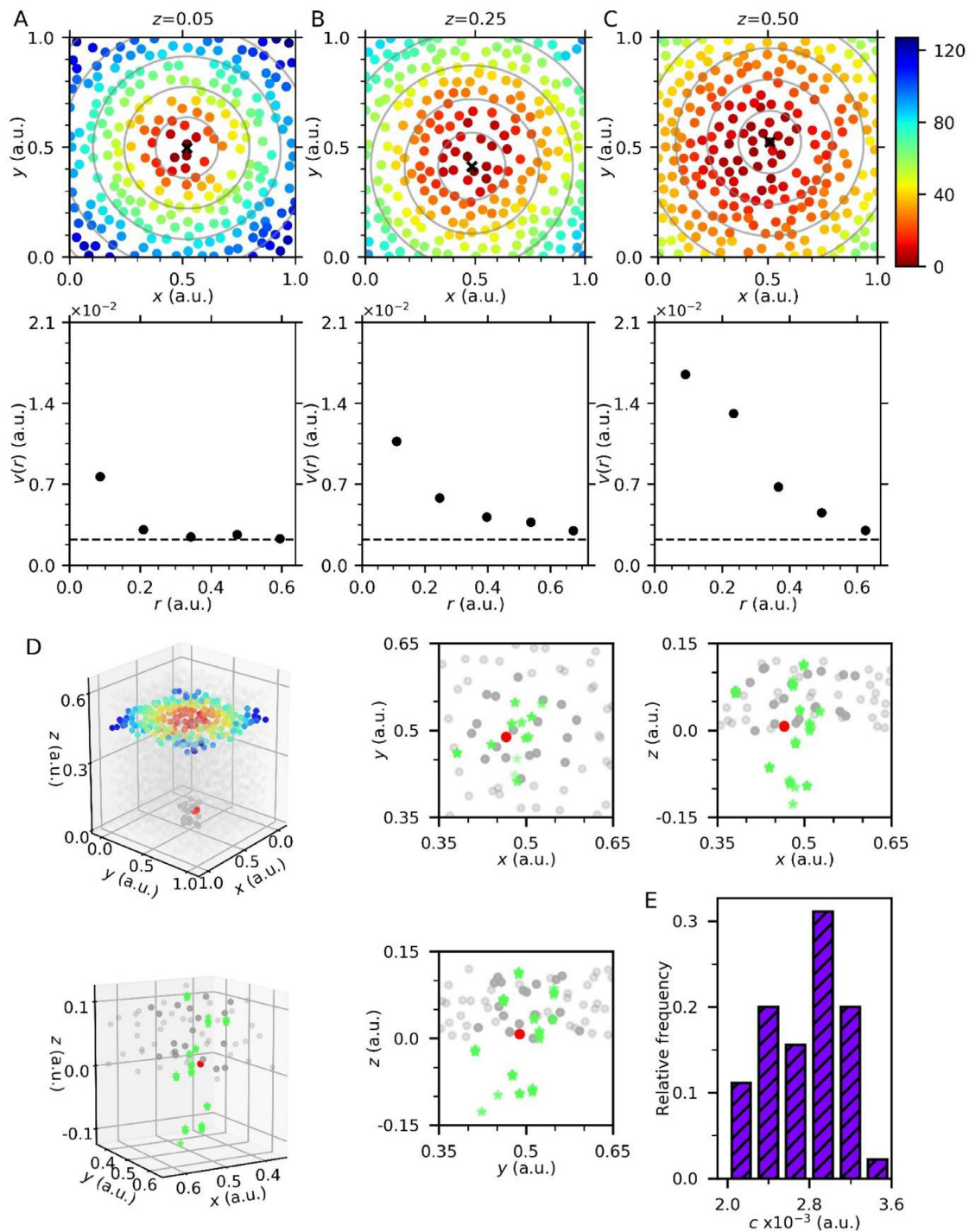
Fig. 6. Cellular activation profiles in different cross-sections in the heterogeneous network of cells (upper panels) at $z=0.05$ (A), $z=0.25$ (B) and $z=0.5$ (C) with indicated starting points (black crosses) and circular sectors (grey circles). The width of each slice was 0.05. The activation times of individual cells are color-coded, as indicated by the color bar. Lower panels feature their corresponding velocity profiles $v(r)$, i.e. velocities determined on the basis of the average activation times in circular sectors and the average distance from the origin. Dashed lines indicate the actual wave front propagation velocity (c), as determined in the pacemaker plane. Upper left panel (D) features the average extracted wave origin position from five analyzed waves (red dot). Dark grey dots signify pacemaker cells, colored dots represent cells in the observed slice and are colored in accordance with their average activation time. Other cells are shown in light grey. The lower left panel (D) shows the extracted wave origins (green dots) from 50 detected waves. Other three panels show the *xz, xy* and *yz* cross-sections of the pacemaker region, respectively. In panel (E) the distribution of extracted wave front velocities (c) from all 50 waves.
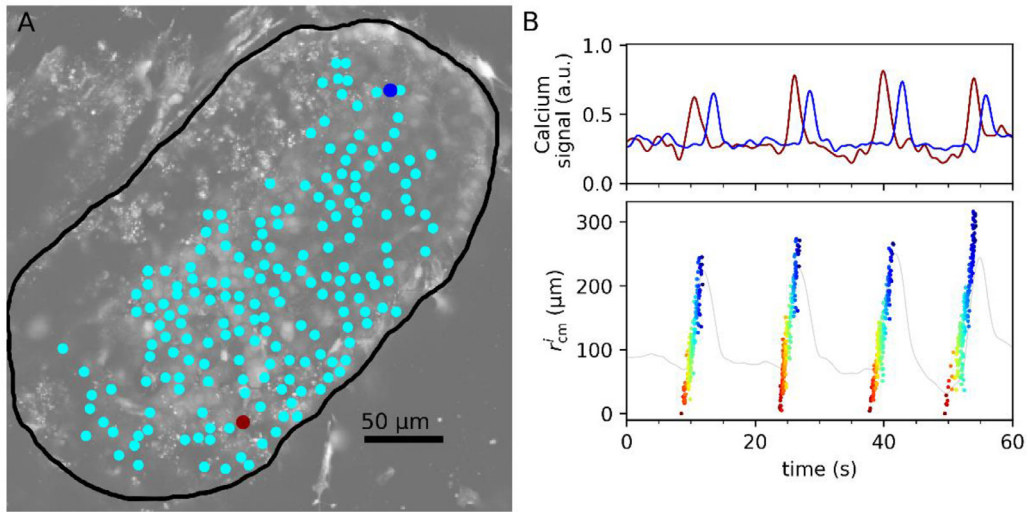
Fig. 7. A) High-resolution image of the pancreatic tissue slice. The black curve signifies the islet of Langerhans and cyan dots indicate individual beta cells. The red and blue dots show the first- and last-responding cells in the given wave, respectively. B) The upper panel shows recorded Ca²⁺ signals of the red and blue cells indicated in panel A with red and blue dots. The lower panel features the activation sequence of cells of 4 subsequent Ca²⁺ waves. Each dot represents the onset of an oscillation and is colored according to its relative activation time. The dots are sorted by their distance (r_{cm}^i) from the starting point of the particular wave.
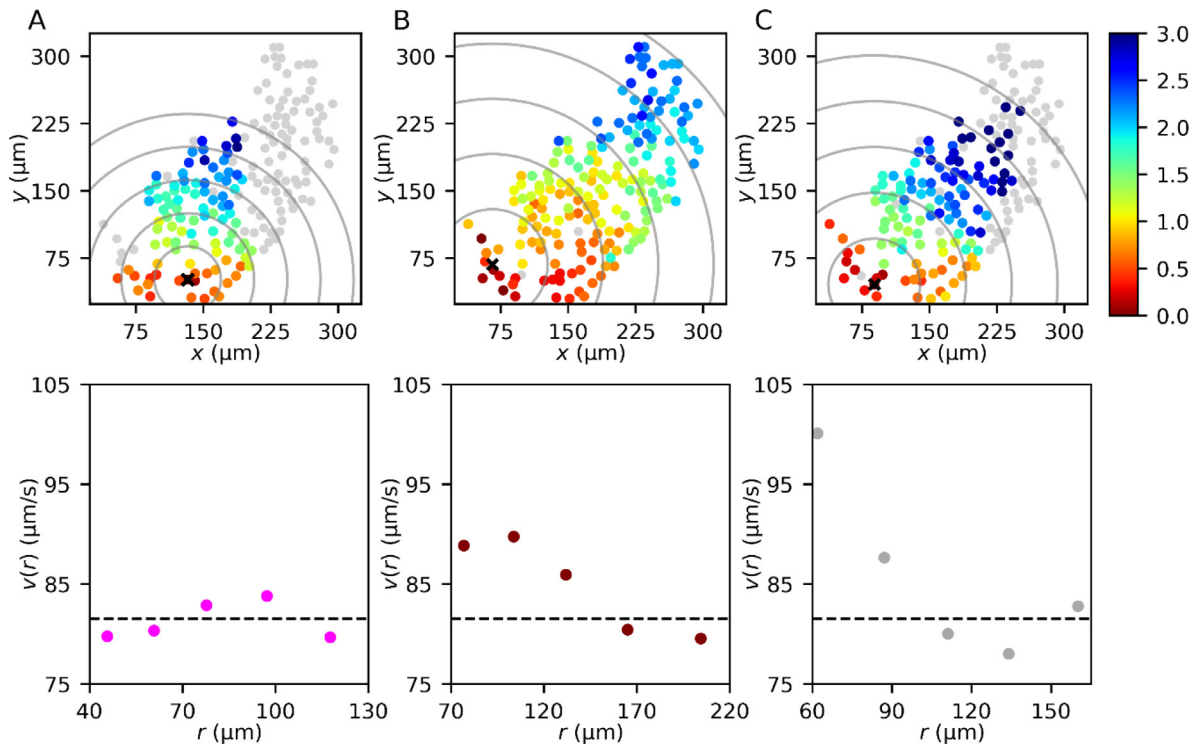
Fig. 8. Experimentally measured color-coded activation sequence of beta cells in the tissue slice (upper panels) with indicated wave impact regions (black cross) and concentric sectors used for the wave velocity calculation after averaging (grey circles). Cells are color-coded in accordance with their relative times of activation, as specified by the color bar. In the lower panels, the corresponding velocity profiles are shown. The dashed line indicates the global average wave front velocity c (see text for details). Note that the colors of dots in lower panels (magenta, dark red and grey) correspond to the colors of determined wave origins in Fig. 9.
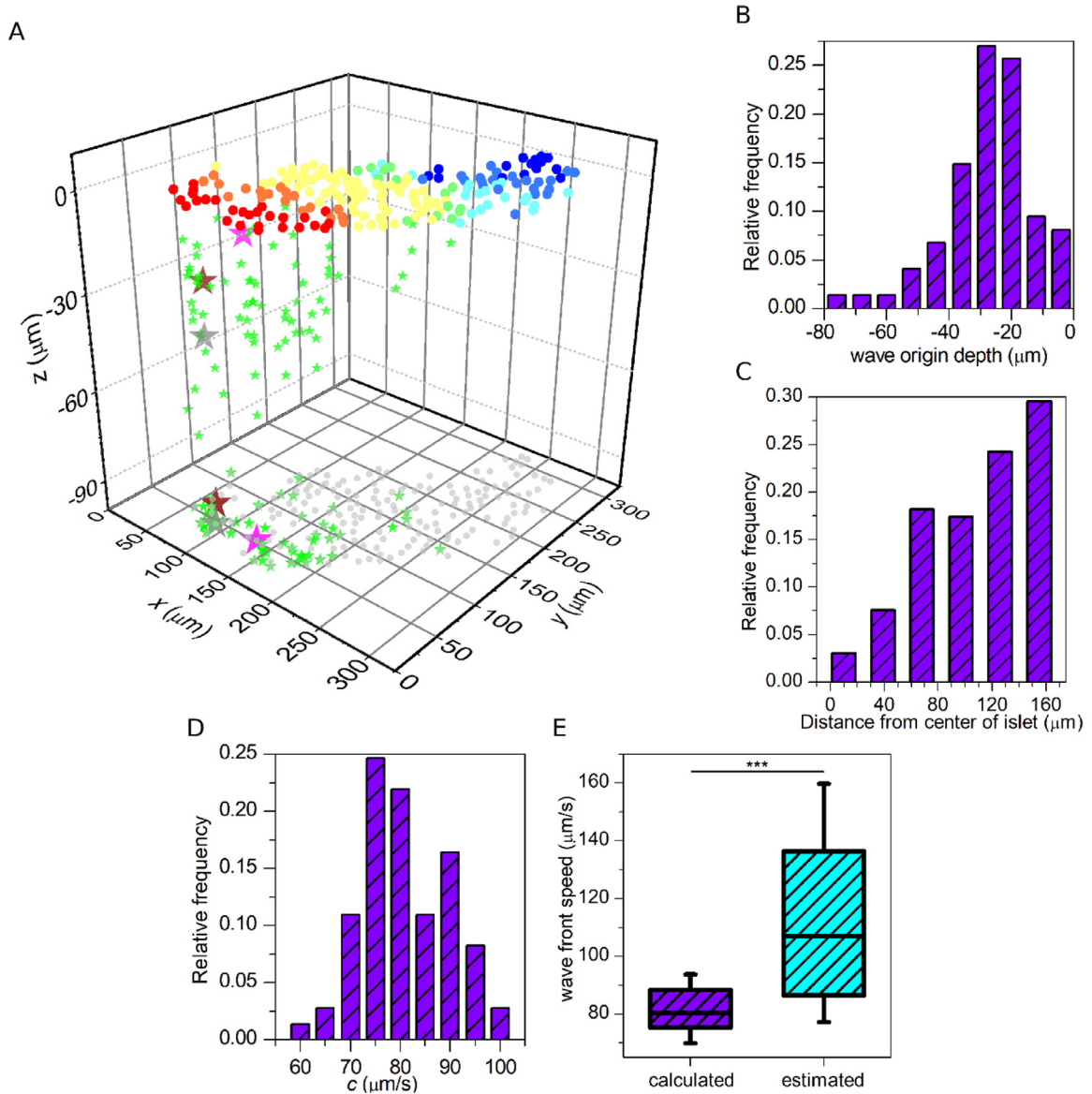
Fig. 9. A) Reconstructed wave initiation regions in the pancreatic islet. The focal plane is placed at $z=0$ and the cells in the observed plane are color-coded in accordance with their average activation rank throughout all 74 waves. Reconstructed wave origins are designated with green stars, except for the three selected waves shown in Fig. 8, where the origins are marked with magenta, dark red and grey. Light grey dots and stars at the bottom are the xy projections of beta cell positions and wave initiator regions, respectively. B) Distribution of calculated depths of wave origins for all detected events. C) Distribution of distances of wave origins from the center of the islet D) Distribution of calculated Ca^{2+} wave velocities from all detected events based on the last 2 points in the distribution. E) Comparison of detected Ca^{2+} wave velocities with our method (violet) and the directly estimated velocity on the basis of the distance and time delay of the first and last sector of the given wave (cyan). Whiskers indicate the 10th and 90th percentile, the box indicates the 25th and 75th percentile and the line indicates the median value. *** $p<0.001$.

pronounced ones, as we address in more detail in the discussion. Nevertheless, the shape of the distribution is quite similar to those we obtained with the heterogeneous multicellular model (see Fig. 6E). To be precise, in both cases the values of velocities were distributed normally with a comparable relative standard deviation (16% for the heterogeneous model and 11% for the experiment). Finally, we compared our calculated values of Ca^{2+} waves with those which were obtained by a more naïve approach employed in previous studies, where the distances between the first and the last activated sector are divided by the corresponding time lag. Both approaches are compared quantitatively in Fig. 9E. Evidently, the simplified estimation of wave velocity yields not only a much broader dispersion of values, but also overestimates the actual Ca^{2+} wave velocity by more than 30 %.

5. Discussion

The combination of a theoretical model, numerical simulations, and experimental data analysis enabled us to quantitatively assess the difference between real Ca^{2+} wave velocities and velocities estimated from signals recorded in an optical plane during fMCI in mouse islets of Langerhans from acute pancreatic tissue slices. The first main finding is that the wave velocities determined from cells at the beginning and end of a wave in the optical plane overestimated more precisely computed values by approximately 30 % or 25 μm/s. The discrepancy was higher for waves originating from a deeper region, whereas for waves that ware triggered close to the focal plane, the obtained values did not significantly differ from values calculated by our framework. We believe that this fact has great practical value for all researchers studying Ca^{2+} waves in 3D cell systems, i.e., isolated islets, beta cell organoids, islets *in vivo*, as well as other tissues. Second, the estimated position of the wave-initiating region was only rarely in the recorded plane, but also practically never below 140 micrometers, which is the slice thickness [91]. The wave initiators were in most cases 10-50 micrometers below the optical plane, which corresponds to 1 to 5 cell layers if we consider the typical size of beta cells. Of course, these findings apply to this particular recording only. A simultaneous 3D calcium imaging would be the method of choice to detect the wave initiators directly and independent of numerical calculations, an endeavor currently not available in technical terms. To assess the positions of initiating cells more precisely within current technical limitations of imaging techniques, measurements of the 3D islet morphology with an extracellular fluorescent dye concurrent with 2D calcium imaging shall provide an interesting outline for future endeavors. It should also be noted that even if the pacemakers, as judged by looking at the recorded plane only, appear to be in the same part of the islet, in reality, they may lie at different depths and this can be revealed by differences in velocity profiles in the recorded plane, with the deeper-lying ones having steeper velocity profiles.

As we previously showed mathematically and experimentally, some waves are localized and thus they never reach the optical plane at which the function is recorded [36]. Therefore, confocal fMCI can only capture global events and local events that reach the optical plane or are initiated in it, thus overestimating the proportion of global events among all events. However, it is reasonable to speculate that the properties of undetected local waves do not differ significantly from the properties of the detected ones. A possible future solution to the above problem is rapid 3D fMCI using fast galvo scanners or adaptive optics.

Since the main focus of this study was to introduce the concept on the basis of which the wave origin and velocity can be firmly estimated, we did not analyze many islets from many different mice in this study, and we also used a single stimulatory concentration of glucose. In the future, a larger number of islets of different sizes, different concentrations of glucose, other physiological and pharmacological secretagogues, and islets from mice and humans with diabetes shall be used. This could help us get a clearer picture of the normal and pathological range of wave velocities, their dependence on islet size and secretagogue dose, and changes in the number and stability of pacemaker regions with disease. This is of especial importance in the light of recent findings suggesting that cells with specialized roles, such as pacemaker cells, could be preferential targets for diabetogenic insults, together with intercellular connectivity supporting Ca^{2+} waves [82,84,89,92–94]. In the mathematical model employed in this study, we did not completely account for all heterogeneities in beta cell function, i.e., differences in metabolism, ion channel densities, and coupling. One possible upgrade of the model presented in this paper would be to incorporate these features. To this end, a more comprehensive biophysical beta cell model could be applied instead of the phenomenological Rulkov model [45]. Additionally, in the present model, we did not completely account for the full complexity of the islet tissue. More specifically, islets comprise many non-beta cells, endothelial cells organized into a complex vessel network, immune cells, and other mesenchymal constituents [43]. Some of these elements could be accounted for by a more realistic beta cell syncytium, possibly extracted from experimental structural recordings. It should be noted that the proposed approach could be applied to other multicellular systems exhibiting calcium waves as well, unless their structure is very anisotropic, such as in the myocardium.

Furthermore, the velocities extracted from experimental data were quite distorted and therefore an adjacent averaging procedure was required to improve the presentation. This is most probably a consequence of the genuine islet morphology, because of which the Ca^{2+} wave fronts are not fully coherent circular structures. Moreover, we excluded 15 out of 89 Ca^{2+} waves from the analysis, because the cellular activation sequence was completely erratic. This could be due to the aforementioned heterogeneity in the islet structure, resulting in intense wave distortions, or due to nearly simultaneous wave initiations from different regions. Especially at higher stimulation levels it might occur more often that global calcium waves are superpositions of multiple waves triggered by different regions of elevated excitability. Since we do not know the positions of origins neither the time lag between the initiations, the actual velocity can in this case not be extracted from the activation profiles. Moreover, the conductance of ATP-dependent ion channels is one of the main regulators of beta cell activity and in realistic conditions, it depends on the cellular metabolism and therefore changes with time. This can, for example, cause that a subpopulation of cells slightly below the focal plane does not get activated in a given calcium event, which would gradually affect the course of the wave front and the resulting velocity profiles. Utilizing more comprehensive multi-component cellular models that take into account multiple facets of beta cell heterogeneity would be a good approach to assess such realistic complex spatiotemporal activity patterns. This would lead to a better understanding of why some experimentally measured activation profiles are more distorted as predicted by our theoretical model and therefore not suitable for such analyses. In a more ambitious scenario, a comprehensive computational model could even provide us valuable information how and at which extent realistic physiological determinants affect the observed activation profiles and this information could be then used to further elaborate the measured results. Finally, as mentioned at the beginning, beta cells

display a rather complex oscillatory Ca^{2+} activity, composed of slow metabolic oscillations, fast bursts, superimposed on the slow oscillations, as well as ultrafast spikes that are superimposed on the bursts and probably correspond to individual action potentials. While our work, similarly as most of the literature in this field, focused on bursts, both the slower metabolic oscillations and the faster spikes could be analyzed using our approach. Such an analysis holds promise to reveal whether the cells that initiate the bursts are also the ones starting the metabolic waves and possibly spiking, as well as to clarify the relationship between pacemakers and hubs [41,84,95].

At present, it is not clear whether human islets behave in a qualitatively and quantitatively similar manner. There is evidence for important differences between the two species [96,97] but also for similarities in the most important structural and functional aspects [76,98]. These have been reviewed in detail recently and are beyond the scope of this work [39,43]. However, it is crucial to keep in mind that for greater translational relevance of research findings human islets should be used in future studies whenever practically feasible.

Declaration of Competing Interest

The authors declare that they have no known competing financial interests or personal relationships that could have appeared to influence the work reported in this paper.

CRediT authorship contribution statement

Marko Šterk: Conceptualization, Software, Formal analysis, Writing - original draft, Visualization. **Jurij Dolenšek:** Conceptualization, Methodology, Writing - review & editing. **Lidija Križančić Bombek:** Methodology, Writing - review & editing. **Rene Markovič:** Software, Writing - review & editing, Visualization. **Darko Zakelšek:** Software, Writing - review & editing. **Matjaž Perc:** Software, Writing - review & editing, Funding acquisition. **Viljem Pohorec:** Methodology, Writing - review & editing. **Andraž Stožer:** Conceptualization, Methodology, Writing - original draft, Writing - review & editing, Supervision, Funding acquisition. **Marko Gosak:** Conceptualization, Software, Writing - original draft, Writing - review & editing, Supervision.

Supplementary materials

Supplementary material associated with this article can be found, in the online version, at doi:10.1016/j.cnsns.2020.105495.

References

[1] Ringer S. A further contribution regarding the influence of the different constituents of the blood on the contraction of the heart. J Physiol 1883;4:29–42. doi:10.1113/jphysiol.1883.sp000120.
[2] Berridge MJ, Bootman MD, Roderick HL. Calcium signalling: dynamics, homeostasis and remodelling. Nat Rev Mol Cell Biol 2003;4:517–29. doi:10.1038/nrm1155.
[3] Tsien RY. Building and breeding molecules to spy on cells and tumors. FEBS Lett 2005;579:927–32. doi:10.1016/j.febslet.2004.11.025.
[4] Rudolf R, Mongillo M, Rizzuto R, Pozzan T. Looking forward to seeing calcium. Nat Rev Mol Cell Biol 2003;4:579–86. doi:10.1038/nrm1153.
[5] Russell JT. Imaging calcium signals in vivo : a powerful tool in physiology and pharmacology. Br J Pharmacol 2011;163:1605–25. doi:10.1111/j.1476-5381.2010.00988.x.
[6] Falcke M. Reading the patterns in living cells −the physics of ca 2+ signaling. Adv Phys 2004;53:255–440. doi:10.1080/00018730410001703159.
[7] Leybaert L, Sanderson MJ. Intercellular Ca(2+) waves: mechanisms and function. Physiol Rev 2012;92:1359–92. doi:10.1152/physrev.00029.2011.
[8] Dupont G, Combettes L, Leybaert L. Calcium dynamics: spatio-temporal organization from the subcellular to the organ level. Int Rev Cytol 2007;261:193–245. doi:10.1016/S0074-7696(07)61005-5.
[9] Røttingen J, Iversen JG. Ruled by waves? Intracellular and intercellular calcium signalling. Acta Physiol Scand 2000;169:203–19. doi:10.1046/j.1365-201x.2000.00732.x.
[10] Jaffe LF. Fast calcium waves. Cell Calcium 2010;48:102–13. doi:10.1016/j.ceca.2010.08.007.
[11] Sneyd J, Charles AC, Sanderson MJ. A model for the propagation of intercellular calcium waves. Am J Physiol Physiol 1994;266:C293–302. doi:10.1152/ajpcell.1994.266.1.C293.
[12] Long J, Junkin M, Wong PK, Hoying J, Deymier P. Calcium wave propagation in networks of endothelial cells: model-based theoretical and experimental study. PLoS Comput Biol 2012;8:e1002847. doi:10.1371/journal.pcbi.1002847.

[13] Dougoud M, Vinckenbosch L, Mazza C, Schwaller B, Pecze L. The effect of gap junctional coupling on the spatiotemporal patterns of Ca2+ signals and the harmonization of Ca2+-related cellular responses. PLOS Comput Biol 2016;12:e1005295. doi:10.1371/journal.pcbi.1005295.

[14] Hraha TH, Westacott MJ, Pozzoli M, Notary AM, McClatchey PM, Benninger RKP. Phase transitions in the multi-cellular regulatory behavior of pancreatic islet excitability. PLoS Comput Biol 2014;10:e1003819. doi:10.1371/journal.pcbi.1003819.

[15] Korotkov AG, Kazakov AO, Levanova TA, Osipov G V. The dynamics of ensemble of neuron-like elements with excitatory couplings. Commun Nonlinear Sci Numer Simul 2019;71:38–49. doi:10.1016/j.cnsns.2018.10.023.

[16] Pedersen MG. Wave speeds of density dependent Nagumo diffusion equations – inspired by oscillating gap-junction conductance in the islets of Langerhans. J Math Biol 2005;50:683–98. doi:10.1007/s00285-004-0304-4.

[17] Potter GD, Byrd TA, Mugler A, Sun B. Communication shapes sensory response in multicellular networks. Proc Natl Acad Sci 2016;113:10334–9. doi:10.1073/pnas.1605559113.

[18] Steinberg BE, Glass L, Shrier A, Bub G. The role of heterogeneities and intercellular coupling in wave propagation in cardiac tissue. Philos Trans R Soc A Math Phys Eng Sci 2006;364:1299–311. doi:10.1098/rsta.2006.1771.

[19] Marhl U, Gosak M. Proper spatial heterogeneities expand the regime of scale-free behavior in a lattice of excitable elements. Phys Rev E 2019;100:062203. doi:10.1103/PhysRevE.100.062203.

[20] Narciso C, Wu Q, Brodskiy P, Garston G, Baker R, Fletcher A, et al. Patterning of wound-induced intercellular Ca 2+ flashes in a developing epithelium. Phys Biol 2015;12:056005. doi:10.1088/1478-3975/12/5/056005.

[21] Kobayashi Y, Sanno Y, Sakai A, Sawabu Y, Tsutsumi M, Goto M, et al. Mathematical modeling of calcium waves induced by mechanical stimulation in keratinocytes. PLoS One 2014;9:e92650. doi:10.1371/journal.pone.0092650.

[22] Tsaneva-Atanasova K, Yule DI, Sneyd J. Calcium oscillations in a triplet of pancreatic acinar cells. Biophys 2005;88:1535–51. doi:10.1529/biophysj.104.047357.

[23] Höfer T. Model of intercellular calcium oscillations in hepatocytes: synchronization of heterogeneous cells. Biophys J 1999;77:1244–56. doi:10.1016/S0006-3495(99)76976-6.

[24] Goldberg M, De Pittà M, Volman V, Berry H, Ben-Jacob E. Nonlinear gap junctions enable long-distance propagation of pulsating calcium waves in astrocyte networks. PLoS Comput Biol 2010;6:e1000909. doi:10.1371/journal.pcbi.1000909.

[25] Kapral R, Showalter K. Chemical waves and patterns editors. Dordrecht: Springer Netherlands; 1995. doi:10.1007/978-94-011-1156-0.

[26] Yang XS. Computational modelling of nonlinear calcium waves. Appl Math Model 2006;30:200–8. doi:10.1016/j.apm.2005.03.013.

[27] Shepelev IA, Vadivasova TE. Variety of spatio-temporal regimes in a 2D lattice of coupled bistable FitzHugh-Nagumo oscillators. Formation mechanisms of spiral and double-well chimeras. Commun Nonlinear Sci Numer Simul 2019;79:104925. doi:10.1016/j.cnsns.2019.104925.

[28] Koenigsberger M, Sauser R, Lamboley M, Bény J-L, Meister J-J. Ca2+ dynamics in a population of smooth muscle cells: modeling the recruitment and synchronization. Biophys J 2004;87:92–104. doi:10.1529/biophysj.103.037853.

[29] Alonso S, Bär M. Reentry near the percolation threshold in a heterogeneous discrete model for cardiac tissue. Phys Rev Lett 2013;110:158101. doi:10.1103/PhysRevLett.110.158101.

[30] Zlochiver S, Muñoz V, Vikstrom KL, Taffet SM, Berenfeld O, Jalife J. Electrotonic myofibroblast-to-myocyte coupling increases propensity to reentrant arrhythmias in two-dimensional cardiac monolayers. Biophys J 2008;95:4469–80. doi:10.1529/biophysj.108.136473.

[31] Kudryashova N, Tsvelaya V, Agladze K, Panfilov A. Virtual cardiac monolayers for electrical wave propagation. Sci Rep 2017;7:7887. doi:10.1038/s41598-017-07653-3.

[32] Cusimano N, Gizzi A, Fenton FH, Filippi S, Gerardo-Giorda L. Key aspects for effective mathematical modelling of fractional-diffusion in cardiac electrophysiology: A quantitative study. Commun Nonlinear Sci Numer Simul 2020;84:105152. doi:10.1016/j.cnsns.2019.105152.

[33] Aslanidi OV, Mornev OA, Skyggebjerg O, Arkhammar P, Thastrup O, Sørensen MP, et al. Excitation wave propagation as a possible mechanism for signal transmission in pancreatic islets of langerhans. Biophys J 2001;80:1195–209. doi:10.1016/S0006-3495(01)76096-1.

[34] Benninger RKP, Zhang M, Head WS, Satin LS, Piston DW. Gap junction coupling and calcium waves in the pancreatic islet. Biophys J 2008;95:5048–61. doi:10.1529/biophysj.108.140863.

[35] Benninger RKP, Hutchens T, Head WS, McCaughey MJ, Zhang M, Le Marchand SJ, et al. Intrinsic islet heterogeneity and gap junction coupling determine spatiotemporal Ca2+ wave dynamics. Biophys J 2014;107:2723–33. doi:10.1016/j.bpj.2014.10.048.

[36] Gosak M, Stožer A, Markovič R, Dolenšek J, Perc M, Rupnik MS, et al. Critical and supercritical spatiotemporal calcium dynamics in beta cells. Front Physiol 2017;8:1106. doi:10.3389/fphys.2017.01106.

[37] Dwulet JM, Ludin NWF, Piscopio RA, Schleicher WE, Moua O, Westacott MJ, et al. How heterogeneity in glucokinase and gap-junction coupling determines the islet [Ca2+] response. Biophys J 2019;117:2188–203. doi:10.1016/j.bpj.2019.10.037.

[38] Nittala A, Ghosh S, Wang X. Investigating the role of islet cytoarchitecture in its oscillation using a new β-Cell cluster model. PLoS One 2007;2:e983. doi:10.1371/journal.pone.0000983.

[39] Dolenšek J, Rupnik MS, Stožer A. Structural similarities and differences between the human and the mouse pancreas. Islets 2015;7:1–16. doi:10.1080/19382014.2015.1024405.

[40] Skelin Klemen M, Dolenšek J, Slak Rupnik M, Stožer A. The triggering pathway to insulin secretion: functional similarities and differences between the human and the mouse β cells and their translational relevance. Islets 2017;9:109–39. doi:10.1080/19382014.2017.1342022.

[41] Benninger RKP, Hodson DJ. New understanding of β-cell heterogeneity and in situ islet function. Diabetes 2018;67:537–47. doi:10.2337/dbi17-0040.

[42] Satin LS, Butler PC, Ha J, Sherman AS. Pulsatile insulin secretion, impaired glucose tolerance and type 2 diabetes. Mol Aspects Med 2015;42:61–77. doi:10.1016/j.mam.2015.01.003.

[43] Skelin Klemen M, Dolenšek J, Slak Rupnik M, Stožer A. The triggering pathway to insulin secretion: Functional similarities and differences between the human and the mouse β cells and their translational relevance. Islets 2017;9:109–39. doi:10.1080/19382014.2017.1342022.

[44] Gosak M, Markovič R, Dolenšek J, Slak Rupnik M, Marhl M, Stožer A, et al. Network science of biological systems at different scales: a review. Phys Life Rev 2018;24:118–35. doi:10.1016/j.plrev.2017.11.003.

[45] Bertram R, Satin LS, Sherman AS. Closing in on the mechanisms of pulsatile insulin secretion. Diabetes 2018;67:351–9. doi:10.2337/dbi17-0004.

[46] Zhang M, Goforth P, Bertram R, Sherman A, Satin L. The Ca2+ dynamics of isolated mouse β-cells and islets: implications for mathematical models. Biophys J 2003;84:2852–70. doi:10.1016/S0006-3495(03)70014-9.

[47] Saeedi P, Petersohn I, Salpea P, Malanda B, Karuranga S, Unwin N, et al. Global and regional diabetes prevalence estimates for 2019 and projections for 2030 and 2045: results from the international diabetes federation diabetes atlas, 9th edition. Diabetes Res Clin Pract 2019;157:107843. doi:10.1016/j.diabres.2019.107843.

[48] Tokarz VL, MacDonald PE, Klip A. The cell biology of systemic insulin function. J Cell Biol 2018;217:2273–89. doi:10.1083/jcb.201802095.

[49] Bertram R, Satin LS, Pedersen MG, Luciani DS, Sherman A. Interaction of glycolysis and mitochondrial respiration in metabolic oscillations of pancreatic islets. Biophys J 2007;92:1544–55. doi:10.1529/biophysj.106.097154.

[50] Rorsman P, Ashcroft FM. Pancreatic β-Cell electrical activity and insulin secretion: of mice and men. Physiol Rev 2018;98:117–214. doi:10.1152/physrev.00008.2017.

[51] Idevall-Hagren O, Tengholm A. Metabolic regulation of calcium signaling in beta cells. Semin Cell Dev Biol 2020. doi:10.1016/j.semcdb.2020.01.008.

[52] Pedersen MG, Bertram R, Sherman A. Intra- and inter-islet synchronization of metabolically driven insulin secretion. Biophys J 2005;89:107–19. doi:10.1529/biophysj.104.055681.

[53] Meda P, Amherdt M, Perrelet A, Orci L. Metabolic coupling between cultured pancreatic B-cells. Exp Cell Res 1981;133:421–30. doi:10.1016/0014-4827(81)90335-9.

[54] Tsaneva-Atanasova K, Zimliki CL, Bertram R, Sherman A. Diffusion of calcium and metabolites in pancreatic islets: killing oscillations with a pitchfork. Biophys J 2006;90:3434–46. doi:10.1529/biophysj.105.078360.

[55] Meissner HP. Electrophysiological evidence for coupling between beta cells of pancreatic islets. Nature 1976;262:502–4. doi:10.1038/262502a0.

[56] Eddlestone GT, Gonçalves A, Bangham JA, Rojas E. Electrical coupling between cells in islets of langerhans from mouse. J Membr Biol 1984;77:1–14. doi:10.1007/BF01871095.

[57] Pérez-Armendariz M, Roy C, Spray DC, Bennett MV. Biophysical properties of gap junctions between freshly dispersed pairs of mouse pancreatic beta cells. Biophys J 1991;59:76–92. doi:10.1016/S0006-3495(91)82200-7.

[58] Dolenšek J, Stožer A, Skelin Klemen M, Miller EW, Slak Rupnik M. The relationship between membrane potential and calcium dynamics in glucose-stimulated beta cell syncytium in acute mouse pancreas tissue slices. PLoS One 2013;8:e82374. doi:10.1371/journal.pone.0082374.

[59] Gosak M, Dolenšek J, Markovič R, Slak Rupnik M, Marhl M, Stožer A. Multilayer network representation of membrane potential and cytosolic calcium concentration dynamics in beta cells. Chaos, Solitons & Fractals 2015;80:76–82. doi:10.1016/j.chaos.2015.06.009.

[60] Benninger RKP, Piston DW. Cellular communication and heterogeneity in pancreatic islet insulin secretion dynamics. Trends Endocrinol Metab 2014;25:399–406. doi:10.1016/j.tem.2014.02.005.

[61] Stamper IJ, Wang X. Integrated multiscale mathematical modeling of insulin secretion reveals the role of islet network integrity for proper oscillatory glucose-dose response. J Theor Biol 2019;475:1–24. doi:10.1016/j.jtbi.2019.05.007.

[62] Singla J, McClary KM, White KL, Alber F, Sali A, Stevens RC. Opportunities and challenges in building a spatiotemporal multi-scale model of the human pancreatic β Cell. Cell 2018;173:11–19. doi:10.1016/j.cell.2018.03.014.

[63] Aslanidi OV, Mornev OA, Vesterager M, Sørensen MP, Christiansen PL. A model for glucose-induced wave propagation in pancreatic islets of Langerhans. J Theor Biol 2002;215:273–86. doi:10.1006/jtbi.2001.2517.

[64] Stamper IJ, Jackson E, Wang X. Phase transitions in pancreatic islet cellular networks and implications for type-1 diabetes. Phys Rev E 2014;89:012719. doi:10.1103/PhysRevE.89.012719.

[65] Hraha TH, Bernard AB, Nguyen LM, Anseth KS, Benninger RKP. Dimensionality and Size Scaling of Coordinated Ca2+ Dynamics in MIN6 β-cell Clusters. Biophys J 2014;106:299–309. doi:10.1016/j.bpj.2013.11.026.

[66] Loppini A, Chiodo L. Biophysical modeling of β-cells networks: Realistic architectures and heterogeneity effects. Biophys Chem 2019;254:106247. doi:10.1016/j.bpc.2019.106247.

[67] Loppini A, Braun M, Filippi S, Pedersen MG. Mathematical modeling of gap junction coupling and electrical activity in human β-cells. Phys Biol 2015;12:066002. doi:10.1088/1478-3975/12/6/066002.

[68] Briant LJB, Reinbothe TM, Spiliotis I, Miranda C, Rodriguez B, Rorsman P. δ-cells and β-cells are electrically coupled and regulate α-cell activity via somatostatin. J Physiol 2018;596:197–215. doi:10.1113/JP274581.

[69] Cappon G, Pedersen MG. Heterogeneity and nearest-neighbor coupling can explain small-worldness and wave properties in pancreatic islets. Chaos An Interdiscip J Nonlinear Sci 2016;26:053103. doi:10.1063/1.4949020.

[70] Loppini A, Capolupo A, Cherubini C, Gizzi A, Bertolaso M, Filippi S, et al. On the coherent behavior of pancreatic beta cell clusters. Phys Lett Sect A Gen At Solid State Phys 2014;378:3210–17. doi:10.1016/j.physleta.2014.09.041.

[71] Westacott MJ, Ludin NWF, Benninger RKP. Spatially organized β-cell subpopulations control electrical dynamics across islets of langerhans. Biophys J 2017;113:1093–108. doi:10.1016/j.bpj.2017.07.021.

[72] Stožer A, Markovič R, Dolenšek J, Perc M, Marhl M, Slak Rupnik M, et al. Heterogeneity and delayed activation as hallmarks of self-organization and criticality in excitable tissue. Front Physiol 2019;10:869. doi:10.3389/fphys.2019.00869.

[73] Santos RM, Rosario LM, Nadal A, Garcia-Sancho J, Soria B, Valdeolmillos M. Widespread synchronous [Ca2+]i oscillations due to bursting electrical activity in single pancreatic islets. Pflügers Arch - Eur J Physiol 1991;418:417–22. doi:10.1007/bf00550880.

[74] Gylfe E, Grapengiesser E, Hellman B. Propagation of cytoplasmic Ca2+ oscillations in clusters of pancreatic β-cells exposed to glucose. Cell Calcium 1991;12:229–40. doi:10.1016/0143-4160(91)90023-8.

[75] Nadal A, Quesada I, Soria B. Homologous and heterologous asynchronicity between identified α-, β- and δ-cells within intact islets of Langerhans in the mouse. J Physiol 1999;517:85–93. doi:10.1111/j.1469-7793.1999.0085z.x.

[76] Quesada I, Todorova MG, Alonso-Magdalena P, Beltrá M, Carneiro EM, Martin F, et al. Glucose induces opposite intracellular Ca 2+ concentration oscillatory patterns in identified α- and β-Cells within intact human islets of langerhans. Diabetes 2006;55:2463–9. doi:10.2337/db06-0272.

[77] Valdeolmillos M, Gomis A, Sánchez-Andrés J V. In vivo synchronous membrane potential oscillations in mouse pancreatic beta-cells: lack of co-ordination between islets. J Physiol 1996;493:9–18. doi:10.1113/jphysiol.1996.sp021361.

[78] Fernandez J, Valdeolmillos M. Synchronous glucose-dependent [Ca 2+] i oscillations in mouse pancreatic islets of Langerhans recorded in vivo. FEBS Lett 2000;477:33–6. doi:10.1016/S0014-5793(00)01631-8.

[79] Jacob S, Köhler M, Tröster P, Visa M, García-Prieto CF, Alanentalo T, et al. In vivo Ca2+ dynamics in single pancreatic β cells. FASEB J 2020;34:945–59. doi:10.1096/fj.201901302RR.

[80] Palti Y, David GB, Lachov E, Mika YH, Omri G, Schatzberger R. Islets of langerhans generate wavelike electric activity modulated by glucose concentration. Diabetes 1996;45:595–601. doi:10.2337/diab.45.5.595.

[81] Chen C, Chmelova H, Cohrs CM, Chouinard JA, Jahn SR, Stertmann J, et al. Alterations in β-cell calcium dynamics and efficacy outweigh islet mass adaptation in compensation of insulin resistance and prediabetes onset. Diabetes 2016;65:2676–85. doi:10.2337/db15-1718.

[82] Salem V, Silva LD, Suba K, Georgiadou E, Neda Mousavy Gharavy S, Akhtar N, et al. Leader β-cells coordinate Ca2+ dynamics across pancreatic islets in vivo. Nat Metab 2019;1:615–29. doi:10.1038/s42255-019-0075-2.

[83] Adams MT, Reissaus CA, Szulczewski JM, Dwulet JM, Lyman MR, Sdao SM, et al. Islet architecture controls synchronous β cell response to glucose in the intact mouse pancreas in vivo. BioRxiv 2019. doi:10.1101/2019.12.11.873471.

[84] Johnston NR, Mitchell RK, Haythorne E, Pessoa MP, Semplici F, Ferrer J, et al. Beta cell hubs dictate pancreatic islet responses to glucose. Cell Metab 2016;24:389–401. doi:10.1016/j.cmet.2016.06.020.

[85] Lei C-L, Kellard JA, Hara M, Johnson JD, Rodriguez B, Briant LJB. Beta-cell hubs maintain Ca 2+ oscillations in human and mouse islet simulations. Islets 2018;10:151–67. doi:10.1080/19382014.2018.1493316.

[86] Rulkov NF. Modeling of spiking-bursting neural behavior using two-dimensional map. Phys Rev E 2002;65:041922. doi:10.1103/PhysRevE.65.041922.

[87] Zhang Q, Galvanovskis J, Abdulkader F, Partridge CJ, Göpel SO, Eliasson L, et al. Cell coupling in mouse pancreatic β-cells measured in intact islets of Langerhans. Philos Trans R Soc A Math Phys Eng Sci 2008;366:3503–23. doi:10.1098/rsta.2008.0110.

[88] Charollais A, Gjinovci A, Huarte J, Bauquis J, Nadal A, Martín F, et al. Junctional communication of pancreatic β cells contributes to the control of insulin secretion and glucose tolerance. J Clin Invest 2000;106:235. doi:10.1172/JCI9398.

[89] Satin LS, Zhang Q, Rorsman P. "Take me to your leader": an electrophysiological appraisal of the role of hub cells in pancreatic islets. Diabetes 2020;69:830–6. doi:10.2337/dbi19-0012.

[90] Speier S, Rupnik M. A novel approach to in situ characterization of pancreatic β-cells. Pflügers Arch - Eur J Physiol 2003;446:553–8. doi:10.1007/s00424-003-1097-9.

[91] Stožer A, Dolenšek J, Rupnik MS. Glucose-Stimulated Calcium Dynamics in Islets of Langerhans in Acute Mouse Pancreas Tissue Slices. PLoS One 2013;8:e54638. doi:10.1371/journal.pone.0054638.

[92] Farnsworth NL, Walter RL, Hemmati A, Westacott MJ, Benninger RKP. Low level pro-inflammatory cytokines decrease connexin36 gap junction coupling in mouse and human islets through nitric oxide-mediated protein kinase Cδ. J Biol Chem 2016;291:3184–96. doi:10.1074/jbc.M115.679506.

[93] Head WS, Orseth ML, Nunemaker CS, Satin LS, Piston DW, Benninger RKP. Connexin-36 Gap junctions regulate in vivo first- and second-phase insulin secretion dynamics and glucose tolerance in the conscious mouse. Diabetes 2012;61:1700–7. doi:10.2337/db11-1312.

[94] Hodson DJ, Mitchell RK, Bellomo EA, Sun G, Vinet L, Meda P, et al. Lipotoxicity disrupts incretin-regulated human β cell connectivity. J Clin Invest 2013;123:4182–94. doi:10.1172/JCI68459.

[95] Rutter GA, Hodson DJ, Chabosseau P, Haythorne E, Pullen TJ, Leclerc I. Local and regional control of calcium dynamics in the pancreatic islet. Diabetes, Obes Metab 2017;19:30–41. doi:10.1111/dom.12990.

[96] Kindmark H, Köhler M, Nilsson T, Arkhammar P, Wiechel K-L, Rorsman P, et al. Measurements of cytoplasmic free Ca 2+ concentration in human pancreatic islets and insulinoma cells. FEBS Lett 1991;291:310–14. doi:10.1016/0014-5793(91)81309-V.

[97] Cabrera O, Berman DM, Kenyon NS, Ricordi C, Berggren P-O, Caicedo A. The unique cytoarchitecture of human pancreatic islets has implications for islet cell function. Proc Natl Acad Sci 2006;103:2334–9. doi:10.1073/pnas.0510790103.

[98] Martin F, Soria B. Glucoseminduced [Ca2+]i oscillations in single human pancreatic islets. Cell Calcium 1996;20:409–14. doi:10.1016/S0143-4160(96)90003-2.